A new methodology for characterizing traction-separation relations for interfacial delamination of thermal barrier coatings

Claudio V. Di Leo[†], Jacques Luk-Cyr[†], Haowen Liu[*†], Kaspar Loeffel[††], Khaled Al-Athel[♭], Lallit Anand[‡†]

[†]Department of Mechanical Engineering
Massachusetts Institute of Technology
Cambridge, MA 02139, USA

[♭]Department of Mechanical Engineering
King Fahd University of Petroleum and Minerals
Dhahran, 31261, Saudi Arabia

November 1, 2013

Abstract

The ability to characterize the interfacial delamination properties of thermal barrier coatings (TBCs) is of great technological importance for lifetime assessment of such coatings under service conditions. The purpose of this paper is to report on our novel experimental-plus-simulation-based approach to determine the relevant material parameters appearing in a traction-separation-type law which should be useful for modeling delamination failures in TBCs. We combine load-displacement measurements obtained from (i) a standard tension experiment; (ii) a novel shear experiment; and (iii) a novel asymmetric four-point bending mixed-mode experiment, with simulations of these experiments using a representative traction-separation law in a finite element program, to extract the needed material parameters in said traction-separation model. The methodology is applied to determine the material parameters for a TBC system (consisting of an air-plasma-sprayed yttria-stabilized-zirconia top-coat and an MCrAlY bond-coat sprayed on a superalloy substrate) which has been isothermally exposed to air at 1100°C for 144 hours prior to testing.

Keywords: Thermal-barrier coatings; Delamination failure; Experimental methods; Cohesive traction-separation model; Finite-element analysis

[*]Now at Intel Corp., 5200 NE Elam Young Parkway., Hillsboro, OR 97124, USA
[†]Now at ALSTOM Power Switzerland Ltd., Brown Boveri Strasse 7., 5400 Baden, Switzerland
[‡]Corresponding author. Tel.: +1-617-253-1635; anand@mit.edu

1 Introduction

A thermal barrier coating is a ceramic/metal bilayer system applied to hot-section blades in gas turbine engines. The ceramic layer, called the *top-coat*,[1] is typically made from yttria-stabilized-zirconia (YSZ) and provides thermal insulation. The metallic layer, called the *bond-coat*, is typically made from an MCrAlY alloy,[2] and provides oxidation protection through the formation of an Al_2O_3-scale, called the *thermally-grown-oxide* (TGO), at the interface between the top-coat and the bond-coat. Two types of deposition processes are typically used to apply the top-coat in gas turbines: electron-beam-physical-vapor-deposition (EB-PVD), and air-plasma-spray (APS). The two techniques produce different top-coat microstructures, with porous APS top-coats being the most commonly used in land-based gas-turbines because of their lower cost. The service life of a TBC is typically limited by spallation of the top-coat.

Many different types of failure modes leading to TBC spallation have been observed in laboratory experiments, as well as upon postmortem examinations of coated turbine blades that have experienced actual service. The most widely observed delamination failures of top-coats which are APS-deposited on MCrAlY bond-coats, typically occur at the bottom of the top-coat, either just above or through the TGO, near the top-coat/TGO interface.

Due to the complexity of the micro-mechanisms leading to degradation of the adherence of TBCs, presently available mechanism-based theories (cf., e.g., Loeffel et al., 2013; Khaled et al., 2013) are not yet sufficiently mature to allow reliable quantitative prediction of the degradation of the delamination strength and toughness of TBCs. This state of affairs is no different from many other areas where fracture mechanics is used to assess structural integrity. As remarked by Hutchinson and Hutchinson (2011), because models of strength and toughness are usually not sufficiently accurate for quantitative predictions — *strength and fracture toughness are properties that are measured, and not predicted*. Thus, at present, an essential component of any lifetime assessment scheme for TBCs must include an *experimental determination* of the delamination strength and toughness of any given TBC system as a function of the relevant thermal history. Fracture-mechanics-based experimental approaches for measuring delamination toughness properties have been reviewed by Hutchinson and Hutchinson (2011).

In contrast to the experimental methods for measuring relevant properties appearing in classical fracture-mechanics models of delamination, here we shall focus our attention on measuring properties appearing in *cohesive interface models* of delamination failures (cf., e.g. Barenblatt, 1959; Dugdale, 1960; Needleman, 1990; Needleman and Xu, 1994; Camacho and Ortiz, 1996; Hutchinson and Evans, 2000). In such models decohesion is regarded as a gradual phenomenon in which separation takes place across a cohesive zone, and is resisted by cohesive tractions. This methodology of modeling fracture requires the specification of interface constitutive parameters, such as the interface stiffness, peak cohesive tractions, and the fracture energy — as represented by the area under the cohesive traction-separation relation. Attractive features of this approach to model delamination fracture are that it is independent of: (a) the far-field geometry of the component containing the interface; (b) the specific constitutive response of the material on either side of the interface; and (c) the extent of the crack growth. Indeed, the location of the evolving crack/delamination front is an *outcome* of the calculations based on this methodology. Cohesive laws have been built into finite element analyses by using *cohesive finite elements*. These surface-like elements bridge nascent cracks, and are compatible with finite element discretizations of the material on either side of a potential crack.

At this stage of research in the literature the material parameters appearing in interface traction-separation laws are the least well-known of the required ingredients for modeling TBC delamination failures using this methodology. There are no standard experimental testing procedures for comprehensively determining the properties in traction-separation relations. The purpose of this paper is to report on our novel experimental-plus-simulation-based approach to determine the relevant material parameters appearing in traction-separation type laws which may be useful for modeling delamination failures in TBCs. Briefly, we use

- load-displacement measurements obtained from three distinct experiments:

  (i) a standard tension-delamination experiment;

[1] In the literature, the ceramic top-coat is often called the TBC. However, we reserve the terminology TBC for the bilayer system composed of the ceramic top-coat and the metallic bond-coat.

[2] Where M stands for Fe, Ni, Co or a combination of these elements.

(ii) a novel shear-delamination experiment; and

(iii) a novel asymmetric four-point bending mixed-mode delamination experiment,

together with

- a numerical implementation of a representative traction-separation law in a finite element program to simulate the three experiments,

and thereby extract the needed material parameters in the traction-separation model.

In this paper we focus our attention on describing our experimental-simulation-based procedure for determining the material properties to *one prior thermal exposure history of an APS-TBC system*. Specifically, we consider a system which has been exposed to 1100° C for 144 hours. We leave a determination of the evolution of these properties with thermal histories to future work.

Further, we emphasize from the outset that it is not the purpose of this paper to propose a new traction-separation model. However, for specificity, we consider a particular existing traction-separation model which is a variant of a model proposed by Camanho and Davila (2002). Such an interface model has been implemented as a built-in feature in the finite element analysis package Abaqus/Standard (2013), and is quite widely used for modeling delamination failures in laminated carbon-epoxy composite materials.

The plan of this paper is as follows. Our new experimental methodology and procedure for characterizing interfacial delamination properties of TBCs is described in Section 2. The interface constitutive model, its numerical implementation and application to determining interfacial properties of TBC are discussed in Section 3. We conclude in Section 4 with some final remarks.

2 Experiments

2.1 Materials

The air-plasma-sprayed TBC system investigated in this paper was prepared for us by colleagues at the Center for Thermal Spray Research at the State University of New York at Stony Brook. A NiCoCrAlY bond-coat[3] with a thickness of 325 μm was applied by high-velocity oxygen fuel (HVOF) on an Inconel 718 superalloy substrate of 2.5mm in thickness. The ceramic top-coat was produced using agglomerated and sintered 8 wt.% yttria-stabilized-zirconia powder[4] and plasma-sprayed on the bond-coat with an 8 mm nozzle.[5] The thickness of the top-coat layer is approximately 350 μm. Prior to spraying, the substrate surface was cleaned with alcohol and grit blasted using #24 alumina grit at a pressure of 80 psi. The bond-coat was strategically sprayed to achieve surface roughness of approximately 7-8 μm Ra.

Fig. 1(a) shows an SEM micrograph of the cross-section of an as-sprayed TBC sample. Since delamination failures of TBC systems in real components occurs after some minimal time in operation, at which point a TGO layer has formed, we have chosen to develop our methodology for characterizing interfacial traction-separation properties on a specimen with an existing TGO layer. Specifically, we have investigated the properties of TBC coupons which have been isothermally exposed to air at 1100°C for 144 hours. Fig. 1(b) shows the cross-section of such a TBC specimen. The TGO layer, approximately 5μm thick, is clearly visible in this figure.[6]

2.2 Tension delamination experiment

One of the simplest and most widely used methods to determine the bond-strength of an interface is a tension experiment (cf., ASTM standard C633-79, Hongyu et al., 2009; Watanabe et al., 2008). The specimens for such an experiment were prepared by first bonding the TBC onto a 3 mm thick 1018 steel substrate, ceramic face down, using a commercial epoxy,[7] and curing the bond at 150°C for 20 minutes. A water-jet machine was then used to to create 5 mm square specimens of the steel/TBC assembly. Next, the specimens were bonded

[3] Coarse Amdry 386-4 layer over dense Amdry 386-2, Sulzer Metco Inc., USA

[4] Metco-204NS, Sulzer Metco Inc., USA.

[5] Sulzer Metco F4 MB torch.

[6] The images were taken using a HITACHI TM3000 scanning-electron-microscope operated at 15kV.

[7] Araldite AW106/HV953

on both sides onto aluminum tension bars, using the same adhesive and curing specifications. A schematic of a sample prepared in this manner is shown in Fig. 2(a). Such specimens were tested in a single-column tabletop Instron 5944 machine, with a load-cell of 2 kN capacity and an accuracy of ±0.5%. Fig. 2(b) shows a close-up image of the specimen in the tension machine. The tension-bars were spray-painted to produce a speckle pattern for measuring their relative displacements using a digital-image-correlation (DIC) apparatus.[8] Such an experiment allows for a measurement of the interfacial stiffness and strength in a pure tensile mode.

The normal stress versus normal relative displacement curves obtained from tension experiments are shown in Fig. 3. Four TBC specimens were tested and their response is reasonably consistent. The normal stress is computed by dividing the measured applied force by the area of the TBC specimen. It can be observed that the response is essentially linear until a peak stress-level is reached, at which point the interface fails abruptly. Fig. 3(a) and Fig. 3(b), respectively, show the error bars in the displacement measurements, and the stress measurements. We attribute the major part of the substantial scatter in the displacement measurements shown in Fig. 3(a) to the inherent noise in the encoder for the stepper-motor used for displacement actuation in the Instron machine.

Figs. 4(a) and (b) show representative SEM micrographs of the bond-coat side fracture surface of the TBC specimen obtained after a tension experiment. Even at low magnification, Fig. 4(a), the TGO is clearly visible as the dark annular regions in the micrograph. At a higher magnification, Fig. 4(b) reveals regions of exposed bond-coat separated from the top-coat by an annular TGO layer. Fig. 5, shows an SEM micrograph of the top-coat side fracture surface of the same specimen. Here, we see a dark circular region of exposed TGO, known as the TGO "cap", which mates one of the exposed bond-coat regions shown in Fig. 4. As shown schematically in Fig. 6, the micrographs in Figs. 4 and 5 reveal that the fracture path proceeds in an alternating fashion between the top-coat, the TGO, and the bond-coat, and *is always near or at the top-coat/TGO/bond-coat "interface"*. We thus conclude that the data in Fig. 3 from our tension experiments reflect the fracture properties of the "interface" and not of either the top-coat or the bond-coat alone.

2.3 Shear delamination experiment

Next, guided by the experiments of Xu et al. (2010), a novel experiment was used to measure the interfacial failure properties in shear.

Specimen preparation was as follows. First, a TBC plate was placed, ceramic face down, onto a sacrificial aluminum substrate and a water-jet cutter was used to cut small 3×6 mm TBC coupons (the cutting jet entering through the superalloy side). Then, multiple $300\,\mu$m wide and $350\,\mu$m deep top-coat "islands" were carefully machined by using a diamond-wire-saw[9] to cut through the top-coat layer. Fig. 7(a) shows a schematic of the TBC sample where the space in-between the top-coat "islands" is the material removed by the diamond wire saw. Note that from a specimen such as the one shown schematically in Fig. 7(a), up to three experiments may be performed since there are three distinct top-coat "islands" whose shear delamination response may be measured. The shear delamination experiments were conducted in a flexure-based precision biaxial-micro-mechanical testing apparatus shown in Fig. 8. Details regarding this apparatus may be found in Gearing (2002). Briefly, a Burleigh Inchworm actuator which can travel over 6.35 mm with 4 nm resolution is used to drive the TBC specimen against a steel blade at a constant velocity of $0.5\,\mu$m/sec until a top-coat "island" is completely sheared off. The relative tangential displacement between the steel blade and the base of the top-coat "islands" is measured using DIC, see Fig. 7(b) where the speckle pattern for such measurements is shown. The tangential reaction force on the steel blade was measured using a flexure-based shear-load-cell. The shear force in this apparatus can be measured with a resolution of 225μN up to 15 N.

Fig. 9 shows shear stress versus tangential displacement curves for three shear delamination experiments. The shear stress is computed by dividing the measured reaction force by the area of the top-coat/bond-coat interface of the island. Given the inherent local variability of the interfaces in TBCs, the three TBC samples that were tested showed reasonably consistent traction-displacement responses in shear.[10] Observe that the

[8] Vic-2D, Correlated Solutions, Inc.

[9] MTI-STX-201.

[10] Note that in contrast to Fig. 3 in tension, the experimentally-measured response in shear is less noisy because of the precision micromechanical apparatus used to conduct the latter experiments.

traction-displacement response in shear consists of an initial linear region, followed by a region of nonlinearity which leads to a "plateau"-like region of "inelastic" deformation, which subsequently ends with complete shear delamination.

SEM micrographs of the bond-coat side fracture surface of the specimen obtained after the shear delamination experiment are shown in Figs. 10(a) and (b), where the two lighter colored regions in Fig. 10(a) correspond to machining marks caused by the diamond-wire saw during sample preparation. A higher magnification image of the bond-coat side fracture surface is shown in Fig. 10(b). Again, as in the tension experiments, the TGO is clearly visible as a dark annular region surrounding a region of exposed bond-coat. On the corresponding top-coat side fracture surface, Fig. 10(c), the TGO "caps" previously discussed are also observed. The SEM micrographs for the shear experiments (Fig. 10), are consistent with those for the tension experiment (Figs. 4 and 5) and clearly suggest a similar fracture path which proceeds in an alternating fashion though the bond-coat, the TGO, and the top-coat, and is always near or on the interface (Fig. 6). Thus, we conclude that in the shear experiments — as in the tension experiments — the measured traction-displacement response reflects the interfacial delamination response of the top-coat/TGO/bond-coat interface.

2.4 Asymmetric four-point bending

Finally, guided by experiments in the literature (cf., e.g., Thery et al., 2009; Zhao et al., 2011a, 2012), four-point bending experiments on *asymmetric* beams were conducted in order to characterize the *mixed-mode* delamination response of a TBC interface.[11]

Specimen preparation is as follows. First, two TBC plates measuring $15 \times 7\,\text{mm}$ and $15 \times 15\,\text{mm}$ (which have been prepared by water-jet-machining, see previous section) are bonded 8 mm apart onto an aluminum substrate,[12] which is used a metal stiffener, and the bond is cured at 150°C for 20 minutes.[13] A second water jet cutting operation is then used to cut three 3 mm thick beams from the layered structure. The result is an asymmetric beam-bending specimen which is shown schematically in Fig. 11(a). Fig.11(b) shows an actual specimen in a four-point bending set-up in a testing machine. We used the flexure-based micro-mechanical testing apparatus shown in Fig. 12 to conduct our experiments. Details regarding this testing machine may be found in Gudlavalleti (2002) and Gudlavalleti et al. (2005). Briefly, an electromagnetic voice-coil actuator which has a stroke of ±12.7 mm and a maximum continuous stall force of 86.2 N is used in order to apply a normal loading with a 0.5 mN resolution. The top rollers and bottom rollers have a span of 9 and 26 mm respectively, with the top rollers centered in between the bottom rollers. The relative displacement between the top and bottom rollers is measured using DIC, while the reaction force on the top rollers is measured using the flexure-based load-cell.

Fig. 13(a) shows the force versus displacement curves for three asymmetric four-point bending experiments. The load initially increases in a linear fashion up to the point where the strain energy available is sufficient to initiate cracking at the interface. At this critical load, crack initiation is observed near the top-coat/bond-coat interface and the behavior becomes non-linear with an observed load plateau. The critical load is $\approx 24\,\text{N}$ and is reached after a relative roller displacement of $\approx 150\,\mu\text{m}$. The load plateau corresponds to a region of rapid and unsteady crack propagation along the interface. When crack growth reaches a steady-state regime (corresponding to the end of the plateau), the load continues to increase as the remaining uncracked beam is deformed in bending.

It is important to note that the machine used in this experiment imposes a *load* on the beam during bending. Thus if the beam loses its load carrying capacity the machine will rapidly push the specimen through to its next stable configuration. This is what is experimentally observed to occur, and is in accordance with the experimental results of Zhao and Shang (2010). This phenomenon is better understood by plotting the displacement versus time behavior as shown in Fig. 13(b). During the fracture process, a sudden displacement jump from $\approx 150\,\mu\text{m}$ to $\approx 250\,\mu\text{m}$ can be observed which suggests an unstable crack burst.

[11] Thery et al. and others use *symmetric* four-point bending configurations. In such experiments, due to the inherent variability of the properties of the interface and the specimen loading, it is difficult to get the delamination to initiate and propagate in a completely symmetrical manner. We bypass such experimental difficulties by using an asymmetrical specimen configuration.

[12] Using Araldite AW106/HV953.

[13] The stiffener increases the elastic energy available for delamination.

Figs. 14(a) and (b), respectively, show SEM micrographs of the bond-coat-side and top-coat-side fracture surfaces. Consistent with our previous observations for the tension and shear experiment, the TGO is visible on the bond-coat side as dark annular material surrounding exposed bond-coat material. On the opposite side, the top-coat fracture surface again shows dark TGO "caps". For all three experiments, the approximate size of those interfacial defects are of the order of 50 μm.

All of the aforementioned experimental observations regarding failure of TBC systems support the idea that fracture proceeds near the top-coat/TGO/bond-coat interface and can be approximately modeled as an interfacial delamination phenomenon due to the "weak" nature of the TGO layer. In the next section, we present a representative traction-separation constitutive theory for modeling interfacial delamination in TBCs.

3 Interface traction-separation constitutive model

There are many different traction-separation-type models which have been proposed in the literature. To fix ideas, consider the schematic of the pure-mode bilinear traction-separation interface constitutive relation (for a two-dimensional situation) shown in Fig. 15 (cf., e.g., Camanho and Davila, 2002). With respect to this figure, (t_N, δ_N) and (t_T, δ_T) represent the normal and tangential components of the traction vector $\mathbf{t}$ and the separation vector $\boldsymbol{\delta}$ at a point of the interface.

- *The parameters K_N and K_T represent the elastic stiffnesses of the interface for normal and shear separation, respectively.*

Damage is taken to initiate when the following criterion is satisfied,[14]

$$\max\left\{\frac{\langle t_N\rangle}{t_N^0}, \frac{t_T}{t_T^0}\right\} = 1. \tag{1}$$

Here,

- *The parameters t_N^0 and t_T^0 denote the values of the interface strengths in the normal and shear directions, respectively.*

Also $\langle x\rangle$ is the Macaulay bracket used to describe the ramp function with value 0 if $x < 0$ and a value x if $x \geq 0$. Thus, no damage is presumed to occur under a purely compressive loading, $(t_N < 0, t_T = 0)$, at the interface. Under continued loading damage grows until final fracture occurs when the following simple *mixed-mode* criterion is satisfied,

$$\frac{G_N}{G_N^c} + \frac{G_T}{G_T^c} = 1. \tag{2}$$

Here,

- *the parameters G_N^c and G_T^c are two additional material properties, which respectively represent the fracture energy of the interface for pure normal and pure shear separations.*

Finally, unloading subsequent to damage initiation is assumed to occur linearly towards the origin. Reloading also occurs along the same linear path until the "softening envelope" is reached. Then, upon further loading, damage will continue until final fracture according to (2).

This interface model has been implemented as a built-in feature in the finite element analysis package Abaqus/Standard (2013). It is the material parameters

$$\{K_N, K_T, t_N^0, t_T^0, G_N^c, G_T^c\} \tag{3}$$

appearing in this model that we shall calibrate using the experiments described in the previous section.

[14] With respect to the particular traction-separation model considered in this paper and depicted schematically in Fig. 15, "initiation of damage" refers to the initiation of microstructural defects at particular values of the normal and tangential tractions which lead to to the degradtion of of the elastic stiffnesses K_N and K_T.

Remark. It is important to note that this traction-separation model does not account for *frictional sliding in shear after failure of the interface*. If after failure the two surfaces of a failed interface come into contact, then such effects are easily accounted in Abaqus/Standard (2013) by allowing for a frictional contact interaction, with a constant Coulomb friction coefficient μ. We shall use this additional feature of Abaqus/Standard (2013) in calibrating the traction-separation model using our experimental data.

3.1 Estimation of the material properties in the traction-separation constitutive model

In order to determine the material parameters $\{K_N, K_T, t_N^0, t_T^0, G_N^c, G_T^c\}$ involved in the traction-separation constitutive model, we have used Abaqus/Standard (2013) to conduct finite-element analyses to simulate the tension, shear, and asymmetric bending experiments discussed in Section 2. We iteratively varied the values of these parameters so as to obtain acceptable matches of the simulated stress (load)-displacement results with the corresponding experimentally-measured results from the three experiments. In all the finite-element simulations discussed below, we made the following modeling assumptions:

- A plane-strain assumption is used to approximate all of the experiments.[15]
- The top-coat, bond-coat, and superalloy substrate are modeled as linear elastic and discretized using four-noded fully-integrated elements (CPE4), while the cohesive zone, that is the bond-coat/top-coat interface, is modeled using four-noded cohesive elements (COH2D4) with zero initial thickness.
- The top-coat is prescribed a Young's modulus $E = 37\,\text{GPa}$ and Poisson's ratio $\nu = 0.18$, while the bond-coat and superalloy substrate are prescribed $E = 200\,\text{GPa}$ and $\nu = 0.29$ (Zhao et al., 2010).
- For interfaces which have failed and can possibly come into contact after failure, such as in the shear and the bending experiments, we have used a value of $\mu = 0.25$ for the friction coefficient between failed interfaces.

The specifics regarding the simulations of each experiment are as follows:

- The finite-element mesh for the tension experiment is shown in Fig. 16(a). The 1018 steel stiffener is modeled as linear elastic ($E = 200\,\text{GPa}$, $\nu = 0.29$) and also discretized using CPE4 elements. The bottom surface AB (bottom of the superalloy) is fixed in space, while a tensile displacement is applied on the top surface CD (top of the 1018 steel).
- The finite-element mesh for the shear experiment is shown in Fig. 16(b). In these simulations, the bottom surface AB of the superalloy is fixed in space while the steel tool (modeled as an analytical rigid surface) is displaced horizontally at a constant velocity against the top-coat "island" until failure of the interface occurs.
- The finite-element mesh for the asymmetric bending experiment is shown in Fig. 16(c). In these simulations, the aluminum stiffener is modeled as an elastic-perfectly plastic material with Young's modulus $E = 69\,\text{GPa}$, Poisson's ratio $\nu = 0.34$, and yield strength $Y_0 = 258\,\text{MPa}$ and discretized using CPE4 elements.[16] Both top and bottom rollers are modeled as analytical rigid surfaces. The top rollers are fixed in space while the bottom rollers are constrained to move only in the vertical direction at a constant velocity. To prevent rigid body motion, a single node immediately underneath the right top roller is constrained from moving horizontally.

The material parameter estimation procedure that we followed is described below:

[15] Plane-strain simulations are used only to reduce the complexity and computational time associated with simulating the actual three-dimensional geometries of the experiments. We have also performed simulations of these experiments using a plane-stress assumption, and the results from these simulations (not shown) were nearly identical to those for the plane strain simulations shown in this paper.

[16] The aluminum stiffener deforms plastically during the experiments.

(i) First, the material parameters defining the normal stiffness and strength were estimated by simulating the tension experiment as

$$K_N \approx 50 \text{ to } 70 \text{ MPa}/\mu\text{m}, \qquad t_N^0 \approx 12 \text{ to } 14 \,\text{MPa}.$$

We note that the value of t_N^0 can be read directly from the experimental results shown in Fig. 3, however the stiffness K_N requires simulating the experiment since the experimental data includes not only the stiffness of the interface but also that of the substrate, bond-coat, top-coat, and steel stiffener.

(ii) Second, the material parameters defining the tangential stiffness and strength were estimated by simulating the shear experiment as

$$K_T \approx 75 \text{ to } 125 \text{ MPa}/\mu\text{m}, \qquad t_T^0 \approx 8 \text{ to } 10 \,\text{MPa}.$$

As in the tension experiment, the value of t_T^0 can be read directly from Fig. 9, while estimation of K_T requires simulating the experiment.

(iii) Using the estimates for the material parameters $\{K_N, t_N^0, K_T, t_T^0\}$ from the tension and shear experiments, we used the simulations of our asymmetric four-point bending experiments to estimate values for $\{G_N^c, G_T^c\}$.

The steps (i), (ii), and (iii) outlined above were repeated until an acceptable fit to the stress (load)-versus-displacement data from all three experiments was obtained.

Fig. 17 (a), (b) and (c) show comparisons of our simulation results against the three different experimental measurements. The simulations reproduce the experimental measurements with reasonable accuracy. Of course, due to the nature of the pure tension and shear experiments, the strain-softening branch is not observed in the experiments, and are thus are not fit well by the simulations. Therefore, the softening portion of the simulated results is only partially shown in Figs. 17 (a) and (b) as a dashed line. The behavior of the softening branches in tension and shear are controlled by the fracture energies G_N^c and G_T^c which are fit based solely to the asymmetric four-point bending experiments. The material parameters for the traction-separation law used to obtain these fits are listed in Table 1.

Table 1: Material parameters for the traction-separation model

K_N (MPa/μm)	t_N^0 (MPa)	G_N^c (J/m^2)	K_T (MPa/μm)	t_T^0 (MPa)	G_T^c (J/m^2)
60	13.5	100	100	9	100

Based on the presumed cohesive law, we may define intrinsic normal and tangetial cohesive lengths

$$\delta_N^f = 2\frac{G_N^c}{t_N^0} \quad \text{and} \quad \delta_T^f = 2\frac{G_T^c}{t_T^0},$$

respectively. For the pure mode behaviors shown schematically in Fig. 15, these length scales correspond to the values of the normal and tangential displacement jumps when the interface completely loses its load carrying capacity. For the material parameters listed in Table 1,

$$\delta_N^f = 14.8 \,\mu\text{m}, \qquad \delta_T^f = 22.2 \,\mu\text{m}.$$

Some Remarks:

1. Note that with the exception of the values of t_N^0 and t_T^0 which are easily estimated directly from the experimental data, the iterative fitting procedure described above and applied to the non-linear problem at hand yield values for the other material parameters which are inherently non-unique. The specific values for the material parameters $\{K_N, K_T, G_N^c, G_T^c\}$ shown in Table 1, represent only one possible fit to the experimental data.

2. Our "shear delamination" experiments **do not** *induce a pure tangential relative displacement δ_T across the interface.* We have found through our simulations that the relative contribution of the normal tangential displacement δ_N to the shear tangential displacement δ_T in the experiment is controlled by the position of the steel tool relative to the "top-coat island." Specifically, the vertical point of contact between the steel tool and the top-coat "island" (see close-up in Fig. 16(b)) induces a moment on the island which induces a normal relative displacement δ_N, and a corresponding normal traction t_N. Fig. 18 shows a result from our simulations, which reflect the actual geometry used in our experiments. This figure shows the normal stress σ_N (solid line) and the tangential stress σ_T (dashed line) at the cohesive interface immediately before damage initiation (this corresponds to a displacement of $\approx 0.35\,\mu$m in Fig. 17(b)). Fig. 18 clearly shows that our shear delamination experiment is not a pure shear experiment, but exhibits some non-negligible mode-mixity. Note that the fact that the delamination experiment is not a pure shear experiment does not affect our material parameter estimation procedure.

3. Note also that in both the experimental and simulated shear stress versus displacement curves shown in Fig. 17(b), after the initial linear response there is some amount of non-linearity. This nonlinearity is a direct result of the geometry of loading, which as mentioned above, leads to a combined tangential and normal relative deformation across the interface. The mixed-mode deformation leads to contributions to the damage evolution by both the the tangential and normal modes, and in turn results in a non-linear behavior of the resulting shear stress versus shear displacement curve.

4. The traction-separation law considered here is not sufficiently rich to account for the plateau-like region observed in the shear delamination experiments; cf. Fig. 17(b). A more refined interface constitutive model which allows for some inelastic deformation might be required in order to capture the full extent of the apparent "plateau" (e.g., some variant of Su et al., 2004; Wei and Anand, 2004).

5. With regards to the asymmetric four-point bending experiments, Fig. 17(c), the simulations predict that there is a decrease in the load carrying capacity of the system after crack initiation, which appears to be in disagreement with the experimental results. However, this discrepancy is a result of the fact that the simulation was carried out under "displacement-control" while the experiment was conducted under "force-control." Thus, the simulations are able to probe states of the system which in the experiment are unstable and thus jumped over. We note that the force level for the "Maxwell-line" computed from the simulation data shown in Fig. 17(c) is 22.2 N; this value lies within experimentally-measured upper value of 25N and lower value of 20N.

4 Conclusions

We have developed a novel experimental-plus-simulation based methodology for characterizing interfacial delamination properties in a representative traction-separation model which should be useful in simulations of delamination failures of TBCs. The experiments consist of obtaining load-displacement measurements obtained form three different experiments:

(i) a standard tension-delamination experiment;

(ii) a novel shear-delamination experiment; and

(iii) a novel asymmetric four-point bending mixed-mode delamination experiment,

SEM observations of the fracture surface of isothermally exposed (144 h at 1100°C) TBC specimens subjected to the tension, shear and bending experiments revealed that interfacial delamination of TBC proceeds with a crack path that travels in an alternating fashion through the top-coat, the TGO, and the bond coat. Which confirms that the experimentally-measured load-displacement curves reflect the interfacial properties of the top-coat/TGO/bond-coat interface and supports the idea that a TBC delamination failure may be modeled as an "interfacial failure" process using traction-separation-type models.

The experimental methodology proposed in this paper, together with the traction-separation model built in the finite element package Abaqus/Standard (2013), provide a pragmatic and straightforward method for determining interfacial properties of micron-dimensioned multi-layered structures such as TBCs. However, much remains to be done. Specifically:

- Substantial further experimentation is required to determine how the interfacial properties evolve as a function of thermal history.
- Further experimentation is also required in order to shed light on (a) the nature of the mode-mixity of interfacial failure, and (b) the role of friction for interfaces which have failed and can possibly come into contact after failure.

Acknowledgements

The authors would like to thank the King Fahd University of Petroleum and Minerals in Dhahran, Saudi Arabia, for partially funding the research reported in this paper through the Center for Clean Water and Clean Energy at MIT and KFUPM under project number R9-CE-08. Partial support from NSF (CMMI Award No. 019646-001) is also gratefully acknowledged. The help of Professor Sanjay Sampath and Dr. Gopal Dwivedi of SUNY Stony Brook in providing us with TBC samples is gratefully acknowledged.

References

Abaqus/Standard, 2013. SIMULIA, Providence, RI.

Barenblatt, G.I., 1959. The formation of equilibrium cracks during brittle fracture: general ideas and hypotheses, axially symmetric cracks. Applied Mathematics and Mechanics (PMM) 23, 622-636.

Camacho, G.T., Ortiz, M. 1996. Computational modeling of impact damage in brittle materials. International journal of solids and structures 33, 2899-2938.

Camanho, P.P., Davila, C.G. 2002. Mixed-mode decohesion finite elements for the simulation of delamination in composite materials. NASA/TM-2002-211737.

Dugdale, D.S., 1960. Yielding of steel sheets containing slits. Journal of the Mechanics and Physics of Solids 8, 100-104.

Gearing, B.P., 2002. Constitutive equations and failure criteria for amorphous polymeric solids. PhD thesis, Massachusetts Institute of Technology.

Gudlavalleti, S., 2002. Mechanical testing of solid materials at the micro-scale. Master's thesis, Massachusetts Institute of Technology.

Gudlavalleti, S., Gearing, B., Anand, L. 2005. Flexure-based micromechanical testing machines. Experimental Mechanics 45, 412-419.

Hongyu, Q., Xiaoguang, Y., Yamei, W., 2009. Interfacial fracture toughness of APS bond coat/substrate under high temperature. Int. J. Fract. 157, 71-80.

Hutchinson, J.W., Evans, A.G., 2000. Mechanics of materials: top-down approaches to fracture. Acta materialia 48(2000), 125-135.

Hutchinson, R.G., Hutchinson, J.W., 2011. Life-time assessment for thermal barrier coatings: Tests for measuring mixed mode delamination toughness. Journal of American Ceramic Society 94, S85-S95.

Khaled, A., Loeffel, K., Liu, H., Anand, A., 2013. Modeling decohesion of a top-coat from a thermally-growing oxide in a thermal barrier coating. Surface & Coatings Technology 222, 68-78.

Loeffel K., Anand L., Gasem, Z.M., 2013. On modeling the oxidation of high-temperature alloys. Acta Materialia 61, 399-424.

Needleman, A., 1990. An analysis of decohesion along an imperfect interface. International journal of fracture 40, 21-40.

Needleman, A., Xu, X.P., 1994. Numerical simulations of fast crack growth in brittle solids. Journal of the Mechanics and Physics of Solids 42,1397-1434.

Su, C., Wei, Y.J., Anand, L., 2004. An elastic-plastic interface constitutive model: application to adhesive joints. International Journal of Plasticity 20, 2063–2081.

Thery, P.Y., Poulain, M., Dupeux, M., Braccini, M., 2009. Spallation of two thermal barrier coating systems: experimental study of adhesion and energetic approach to lifetime during cyclic oxidation. Journal of Materials Science 44, 1726-1733.

Watanabe, M., Kuroda, S., Yokoyama, K., Inoue, T., Gotoh, Y., 2008. Modified tensile adhesion test for evaluation of interfacial toughness of HVOF sprayed coatings. Surface and Coatings Technology 202(9), 1746-1752.

Wei, Y.J., Anand, L., 2004. Grain-boundary separation and sliding: application to nanocrystalline materials. Journal of the Mechanics and Physics of Solids 52, 2587-2616.

Xu, Z.H., Yang, Y., Huang, P., Li, X. 2010. Determination of interfacial properties of thermal barrier coatings by shear test and inverse finite element method. Acta Materialia 58(18), 5972-5979.

Zhao, P.F., Shang, F.L., 2010. Experimental study on the interfacial delamination in a thermal barrier coating system at elevated temperatures. Journal of Zheijian university 11(10), 794-803.

Zhao, P.F., Sun, C.A., Zhu, X.Y., Shang, F.L., Li, C.J., 2010. Fracture toughness measurements of plasma-sprayed thermal barrier coatings using a modified four-point bending method. Surface and Coatings Technology, 204, 4066-4074.

Zhao, P.F., Li, X.D., Shang, F.L., Li, C.J., 2011a. Interlamellar cracking of thermal barrier coatings with TGOs by non-standard four-point bending tests. Materials Science and Engineering: A 528(25), 7641-7647.

Zhao, Y., Shinmi, A., Zhao, X., Withers, P. J., Van Boxel, S., Markocsan, N., Nylen, P., Xiao, P., 2012. Investigation of interfacial properties of atmospheric plasma sprayed thermal barrier coatings with four-point bending and computed tomography technique. Surface and Coatings Technology 206(23), 49224929.

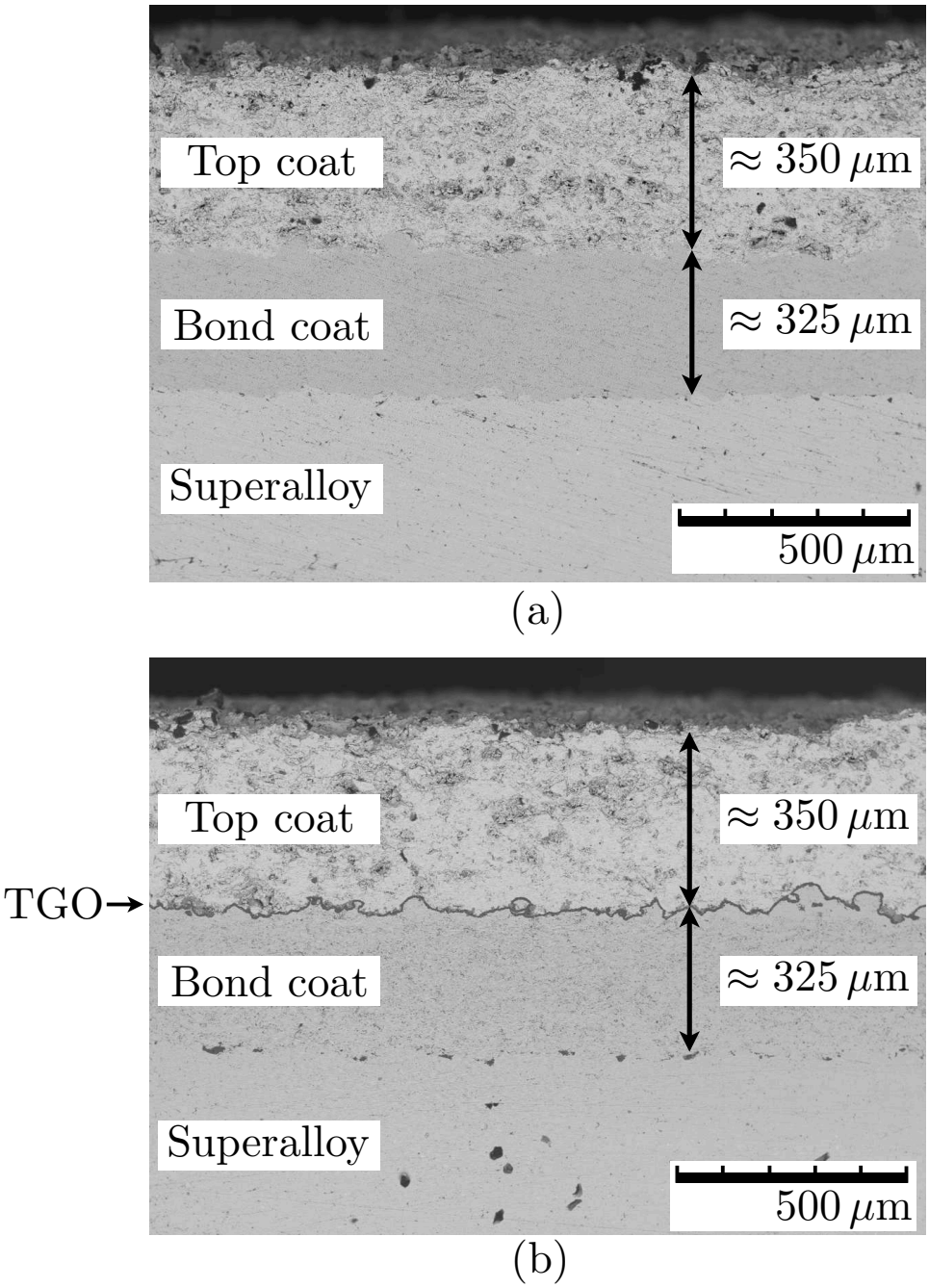

Figure 1: SEM micrograph of the cross-section of a TBC: (a) an as-sprayed specimen, and (b) an isothermally exposed specimen (144 h at 1100°C).

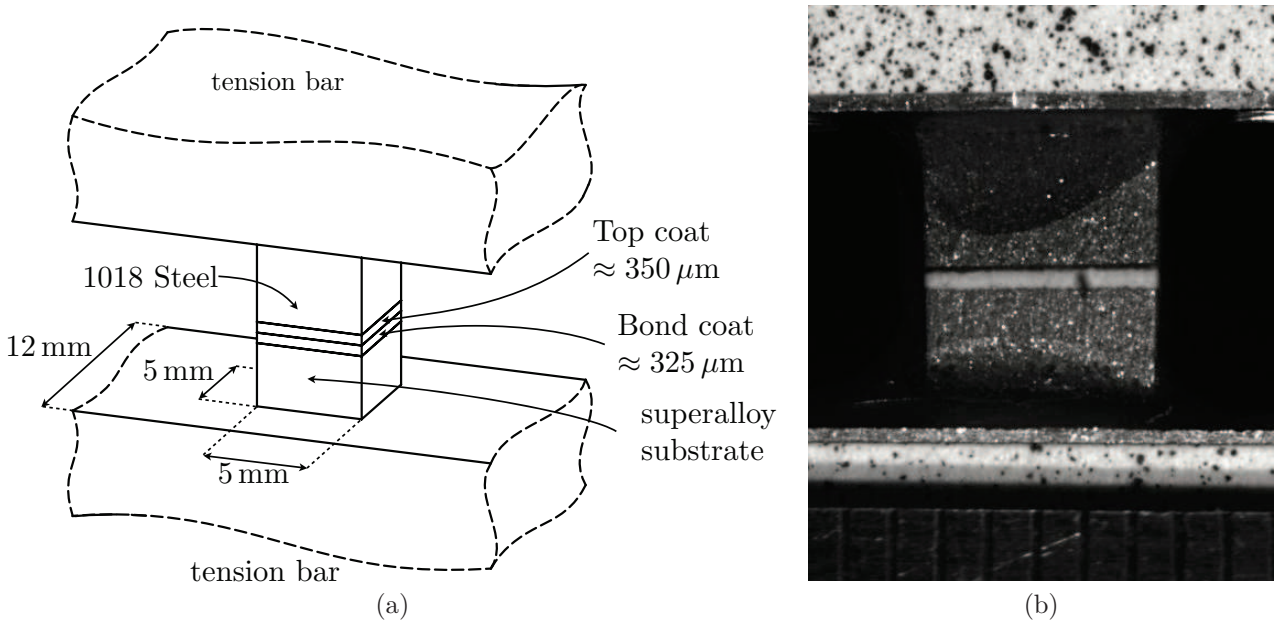

(a) (b)

Figure 2: Tension experiment: (a) Schematic of the tension specimen with dimensions. (b) Close-up of the tension specimen in the low-load Instron 5944 machine.

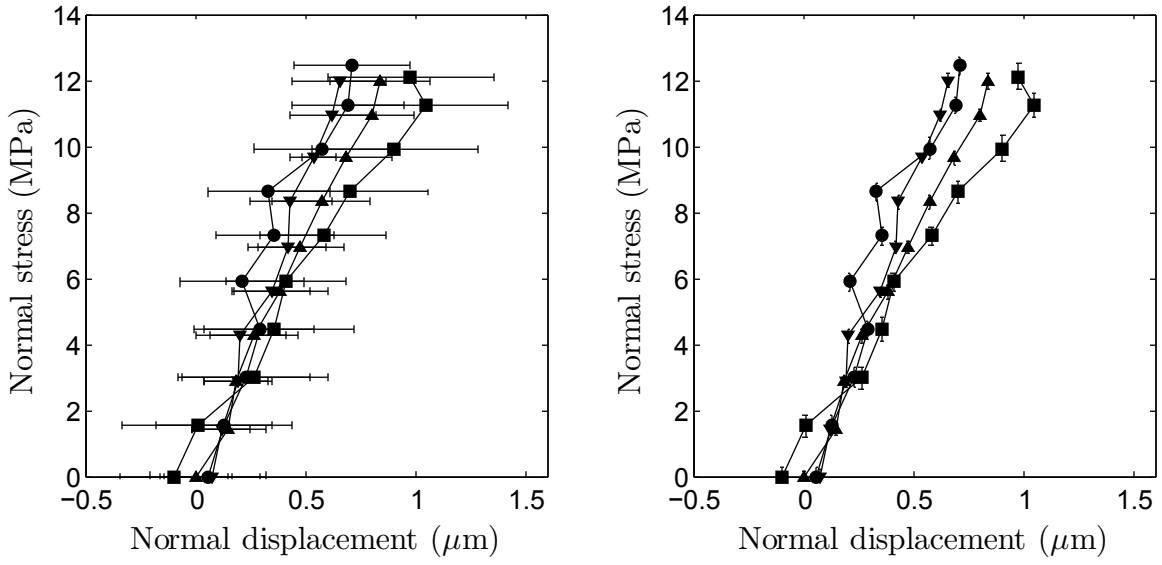

(a) (b)

Figure 3: Stress versus displacement curves from four tension experiments: (a) with error bars for the displacement measurements; and (b) with error bars for the stress measurements. Error bars correspond to one standard deviation on an average taken from ≈ 40 data points.

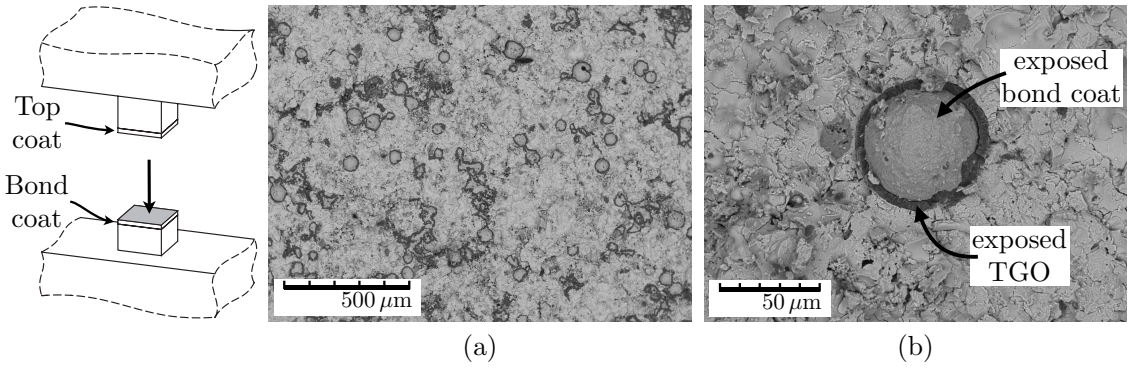

Figure 4: SEM micrographs of the tension fracture surface facing the bond-coat side of the specimen: (a) low magnification, and (b) high magnification. (b) highlights regions of exposed bond coat surrounded by rings of thermally grown oxide (TGO).

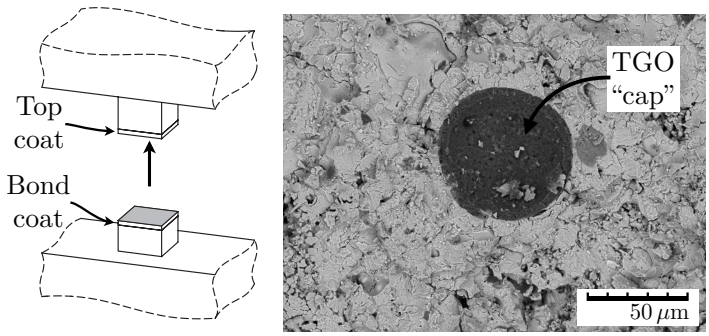

Figure 5: SEM micrograph of the tension fracture surface facing the top-coat side of the specimen. The micrograph highlights a region of exposed TGO, referred to as the “TGO cap”, which matches regions of exposed bond-coat on the opposing fracture surface.

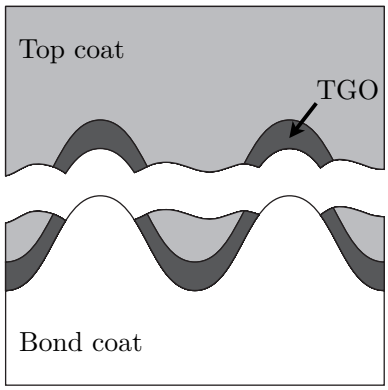

Figure 6: Schematic of the experimentally observed fracture path.

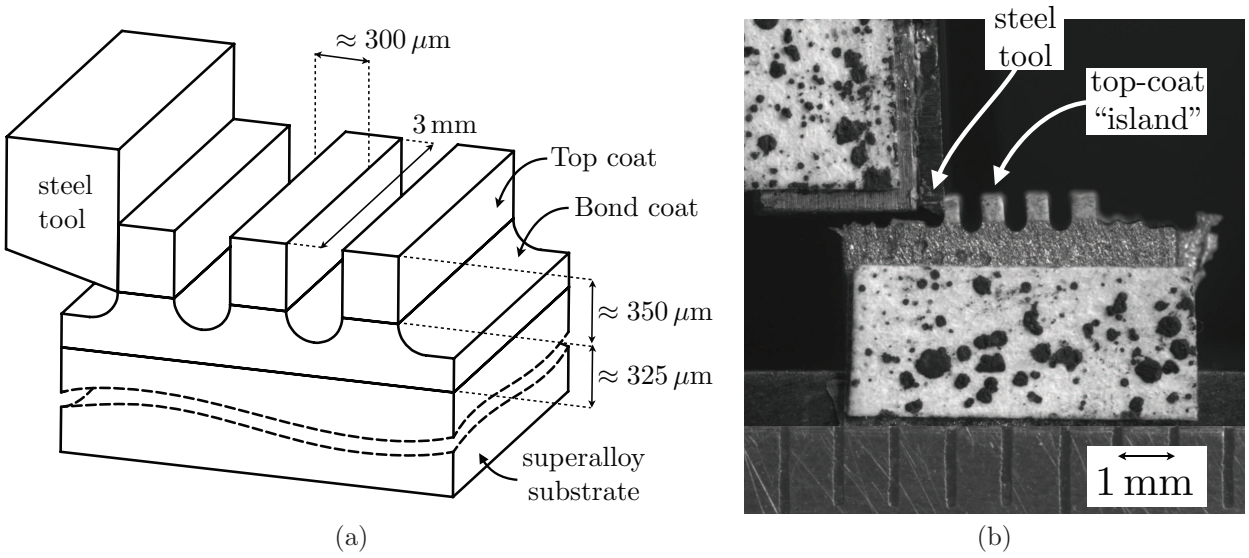

(a) (b)

Figure 7: Shear delamination experiment. (a) Schematic of the shear specimen with dimensions. (b) Close-up of the shear specimen in the testing machine.

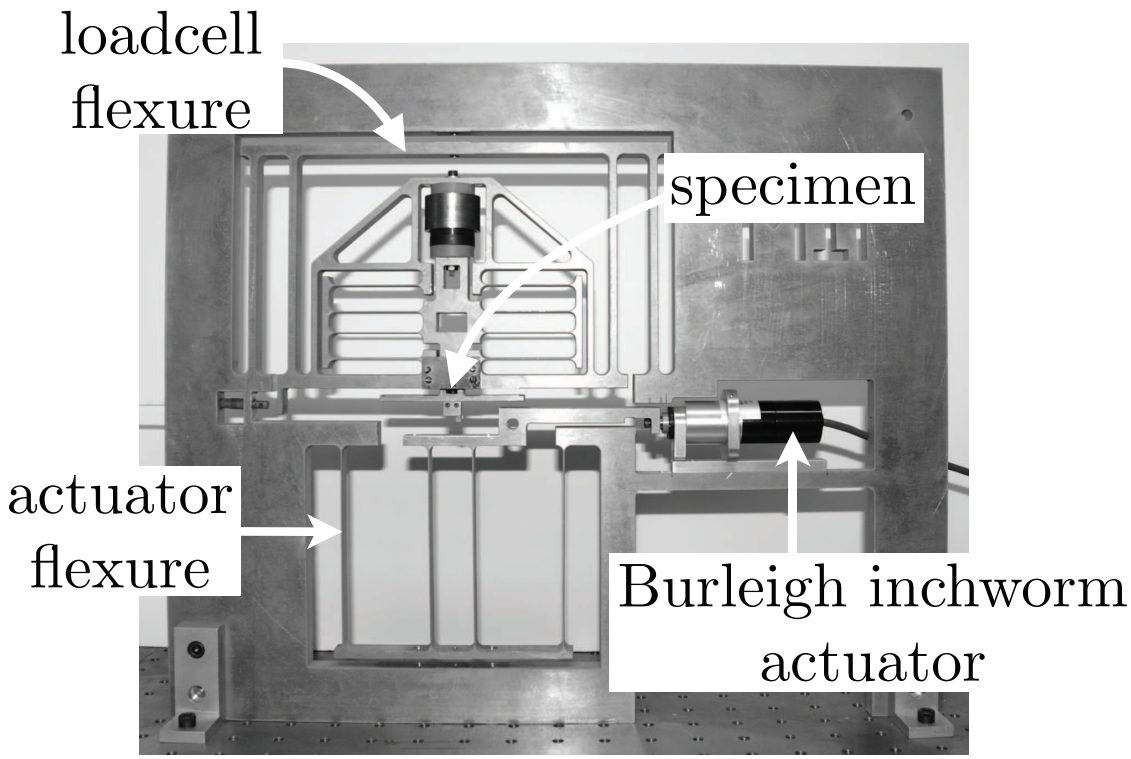

Figure 8: Micromechanical biaxial apparatus used in the shear delamination experiments.

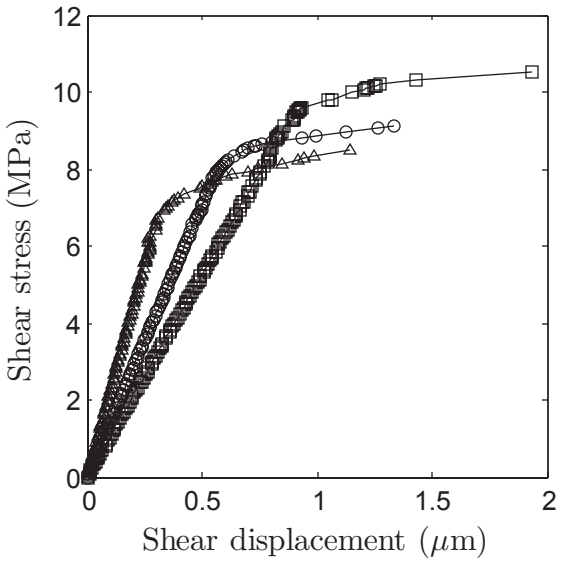

Figure 9: Shear stress versus shear displacement curves from three shear delamination experiments.

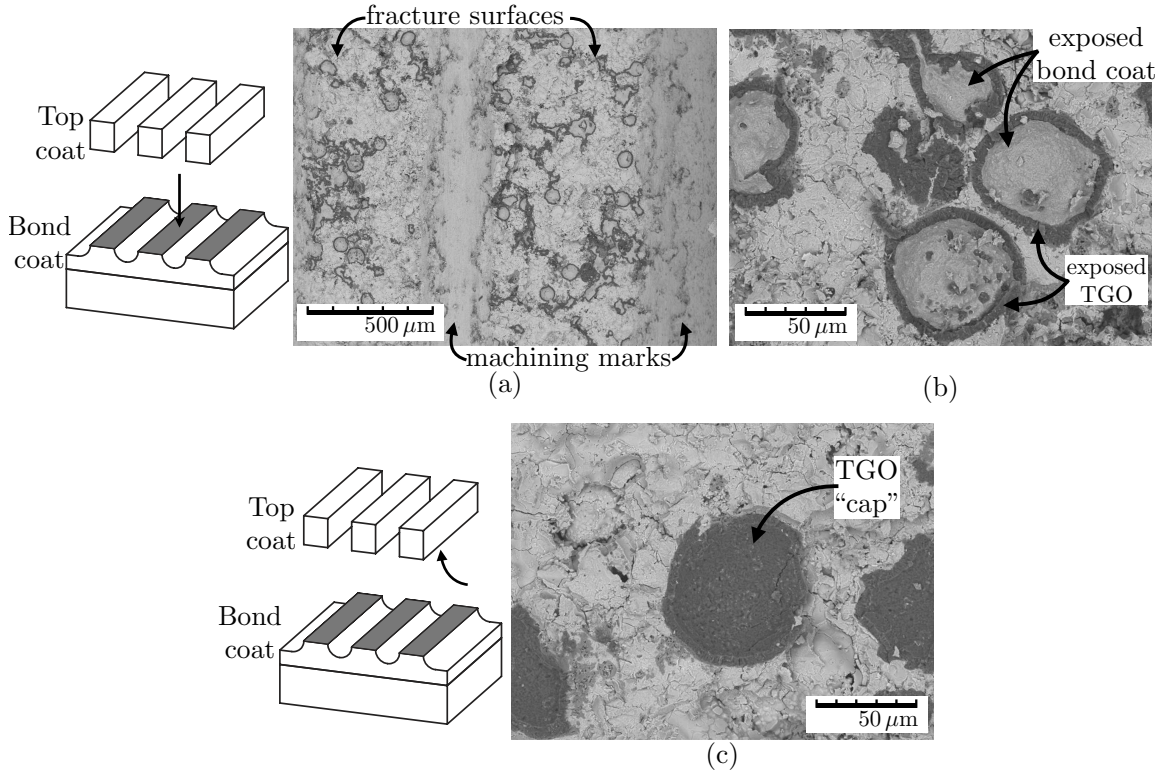

Figure 10: SEM micrographs of the shear delamination fracture surfaces. (a) and (b) show fracture surfaces facing the bond-coat side, while (c) shows a fracture surface facing the top-coat side of the specimen.

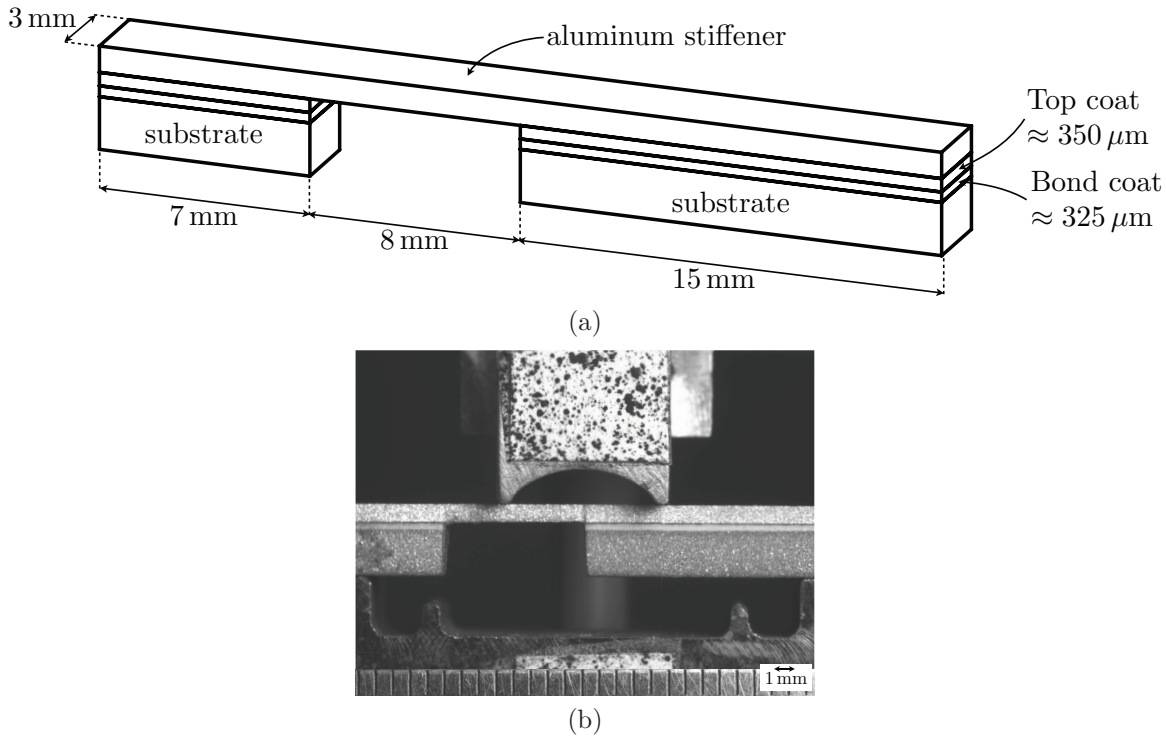

Figure 11: Four-point bending experiment. (a) Schematic of the bending specimen with dimensions. (b) Close-up of the bending specimen in the testing machine.

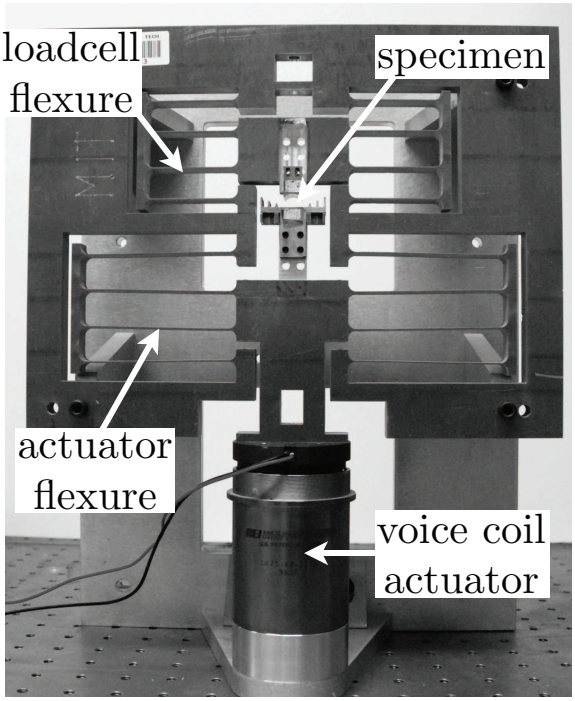

Figure 12: Micro-mechanical apparatus used in four-point bending experiments.

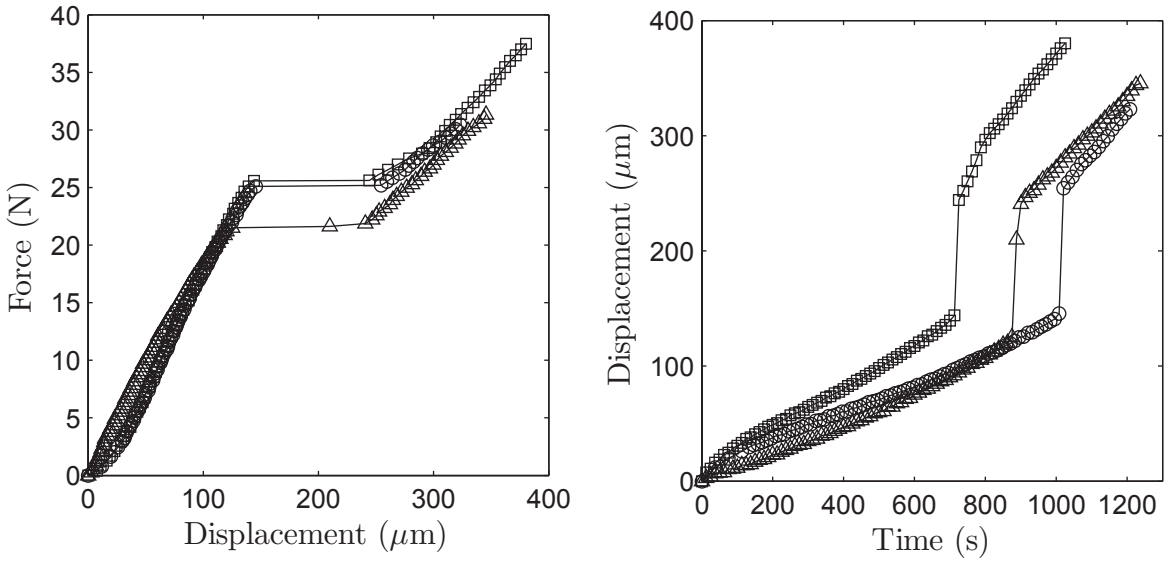

(a) (b)

Figure 13: Asymmetric four-point bending results for three experiments. (a) force vs. displacement response, and (b) displacement vs. time response.

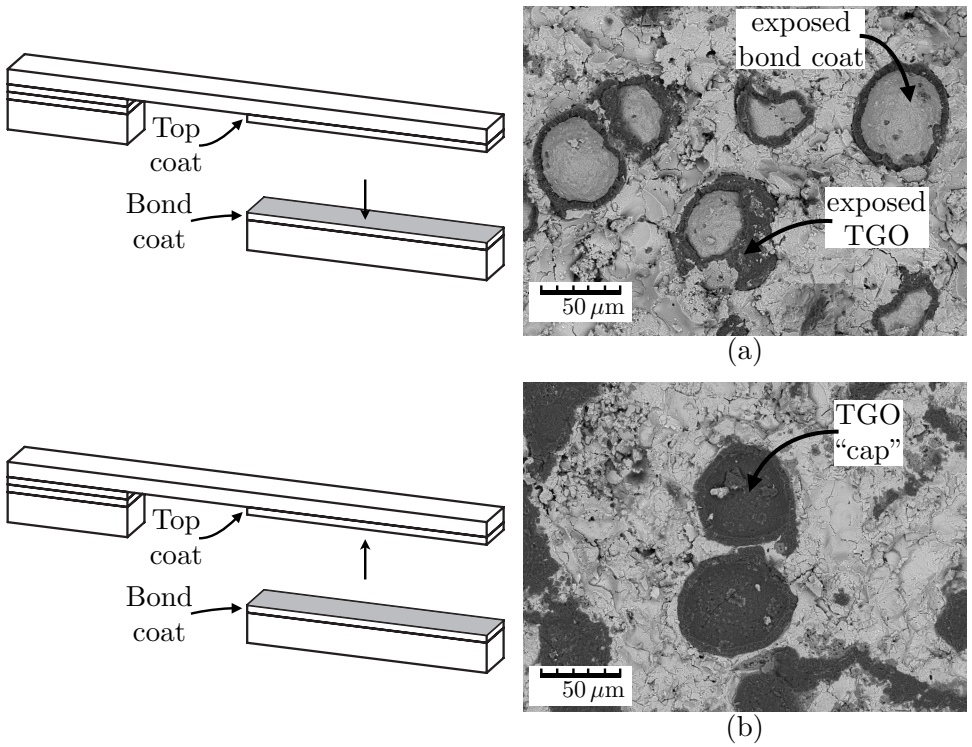

Figure 14: SEM micrographs of the asymmetric four-point bending fracture surfaces. (a) Shows a fracture surface facing the bond-coat side, while (b) shows a fracture surface facing the top-coat side of the specimen.

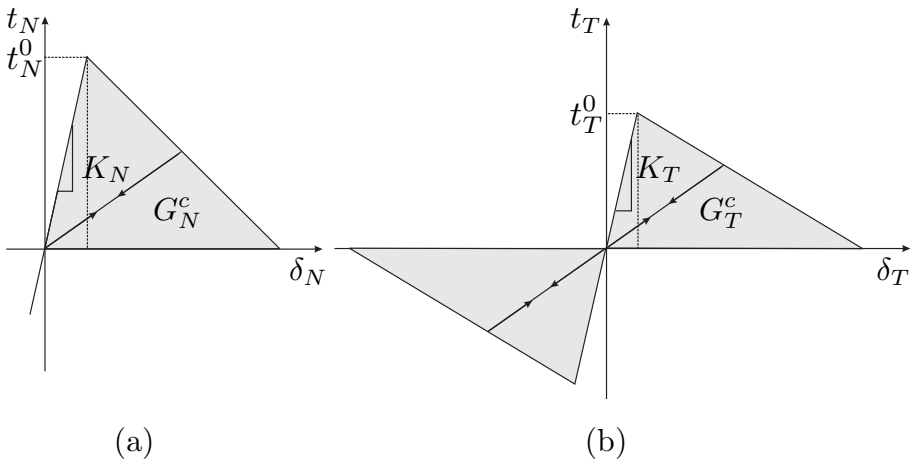

Figure 15: Schematic of the bilinear traction-separation interface constitutive relation, showing (a) the pure normal response (no tangential deformation), and (b) the pure shear response (no normal deformation).

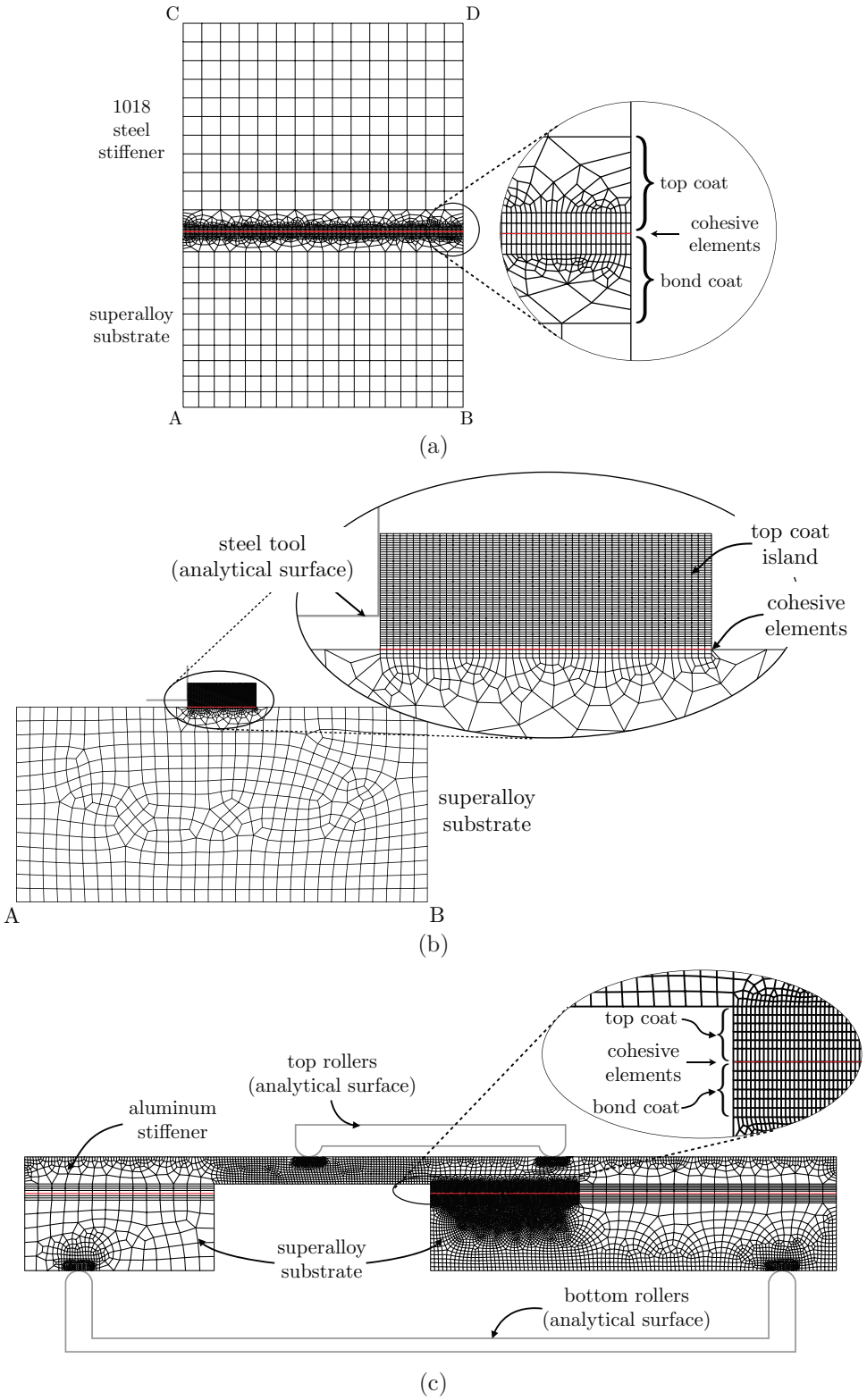

Figure 16: Simulation domain and finite-element meshes for (a) simulations of the tension experiment, (b) simulations of the shear delamination experiments, and (c) simulations of the asymmetric four-point bending experiments. The red line in each mesh highlights the cohesive elements used to model interfacial failure.

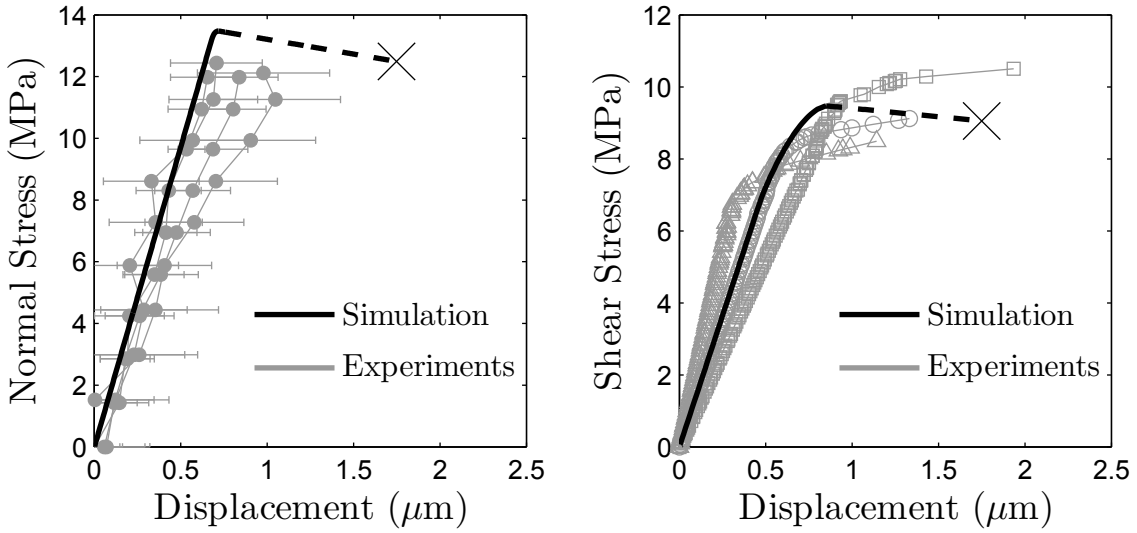

(a) (b)

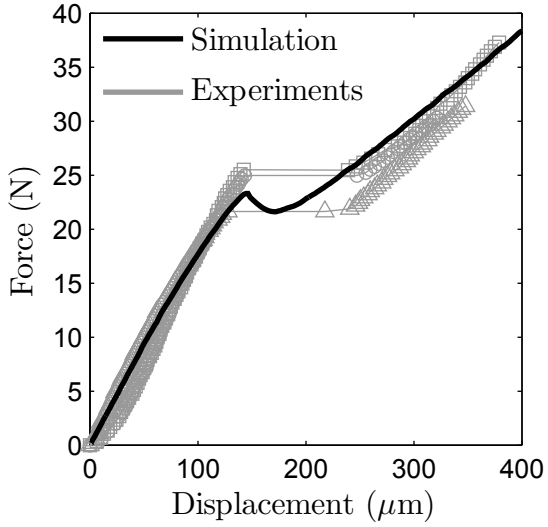

(c)

Figure 17: Simulation fit (black line) and experimental results (gray lines) for (a) normal stress vs. normal displacement for the tension experiments and simulation, (b) shear stress vs. shear displacement for the shear delamination experiments and simulation, and (c) force vs. displacement for the asymmetric four-point bending experiments and simulation.

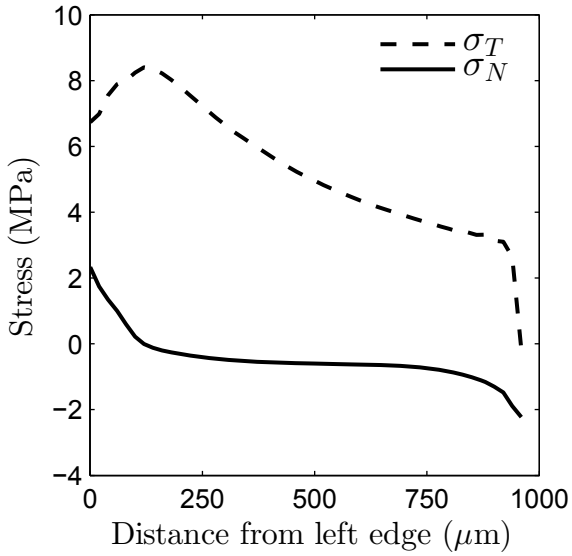

Figure 18: Normal (solid line) and shear (dashed line) stress at the cohesive-interface before damage initiation as a function of the distance from the left edge of the cohesive-interface.